Deconvolving the Rocking Curve

Cecilia Andersson

Supervised by Greg Falzon

Flinders University

Analyser-based X-ray Imaging (ABI) offers the capability to obtain images of internal tissue structures not available via conventional means of X-ray imaging. Measuring important physical quantities such as the scattering distribution requires specialised scientific instrumentation and accurate mathematical deconvolution. Standard deconvolution algorithms such as Wiener deconvolution and t-SVD deconvolution are currently utilised in practice, however such approaches limit capabilities of the ABI technique. A wavelet deconvolution method was investigated to explore its potential benefits under high instrument noise scenarios, such as those that might be encountered with less expensive instrumentation or alternatively under low-dose exposure constraints. Quantitative and qualitative comparisons of a simulated ABI system indicates that the wavelet deconvolution approach is promising with significant improvements over the t-SVD algorithm.
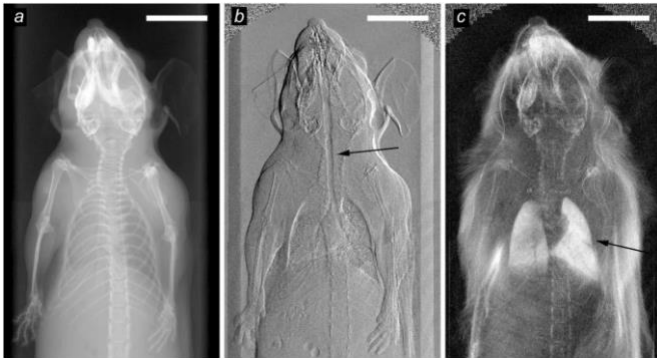
Introduction

Figure 1: Multiple reconstructed images of a mouse obtained with Analyser-Based X-ray Imaging, where (a) shows X-ray absorption, (b) shows X-ray phase-contrast, and (c) shows dark field scatter imaging (Bech et al., 2013).

Analyser-based X-ray imaging (ABI) utilises high precision scientific instrumentation in the form of a monochromatic synchrotron X-ray source, a custom-design analyser crystal and highly sensitive X-ray detectors. The ABI technique provides detailed insights not available with standard X-ray imaging techniques. Figure 1 (a)-(c) demonstrates the capability of ABI to access absorption (standard approach), phase-contrast and scatter information. Phase-contrast imaging visually represents the phase-shifts in a sample, that is, how the crest of the X-ray wave changes rather than its amplitude. This is a form of X-ray imaging, where changes in X-ray phase produce the image rather than the amount of X-ray absorbed (Endrizzi, 2018). Phase-contrast imaging produces high quality images which differentiates between soft tissue better than traditional X-ray imaging, hence it has important medical applications (Zhou & Brahme, 2008). Refer to Figure 1(b) where soft-tissue structures such as the thorax and boundaries of other internal organs such as the lungs are visible. Scatter images can also be obtained through the 'scattering' of X-rays as they encounter micro-structures within the sample. Figure 1(c) demonstrates an X-ray scattering image, note that internal structures such as the lungs are highly visible.

Major ABI X-ray imaging applications include those which are not feasible with standard X-ray imaging. For example, highly detailed imaging and detection of breast cancer; imaging of cartilage and joint structures for arthritis, and imaging of the lung tissue (Pryor et al., 2020). A limitation of the ABI X-ray imaging approach is that there are only a handful of

facilities across the world with access to suitable technology and expertise to perform this advanced form of X-ray imaging.
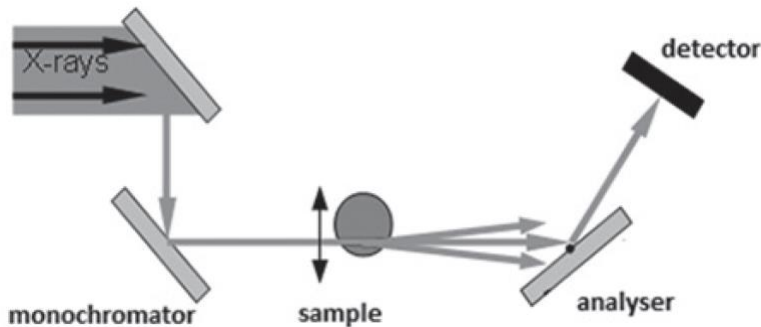

Figure 2: Analyser-based phase contrast imaging set-up (Agrawal et al., 2017).

Figure 2 displays the experimental configuration of the ABPCI (Analyser-based phase contrast imaging) technique, which is a specific form of ABI X-ray imaging used in this project. The ABPCI utilises an 'analyser crystal' as a key component in the detection of X-ray phase. A synchrotron X-ray source illuminates a monochromator, to select a single wavelength to illuminate the sample. Those X-rays encountering the sample are absorbed, scattered, and undergo phase-shifts. An analyser crystal is utilised post-sample filter out X-rays from all but specific angles, rotation of the monochromator across a range of specific angles ensures that only Bragg reflected X-rays, X-ray reflections particularly from crystal structures, are recorded by the detector (Endrizzi, 2018; Kitchen et al., 2010). This process allows the angular distribution of phase-shift and scattering induced by the sample to be assessed. The system described in Figure 2 is one-dimensional, in practical settings, separate one-dimensional systems (often up to 1 million systems) are described for each pixel in order to produce images.

The ABPCI experimental procedure involves recording X-ray detector intensity with no sample present, this allows the effect of the analyser crystal of be understood and is called the rocking curve $I_{ac}(\theta)$. The X-ray detector intensity $I_{exp}(\theta)$ with both the analyser and sample is then recorded, allowing X-ray absorption, phase, and scattering information to be extracted. The scattering distribution of the sample, $\rho(\theta)$, acts in combination with the rocking curve, $I_{ac}(\theta)$, to produce the observed detector intensity $I_{exp}(\theta)$.

The scattering distribution, $\rho(\theta)$, provides important information concerning the micro-structure of the sample, it has been used to develop highly accurate diagnostics of breast tissue malignancy and to understand fundamental science relating to brain cancer spread (Taba et al., 2018). In this project, there is particular interest in understanding the distribution of gas within lungs, in order to better understand and treat respiratory diseases such as COVID-19.

The experimentally observed intensity is modelled as a convolution between the rocking curve and the sample scattering distribution. In general, a convolution is a combination of two functions that produce a third function. In this project, the rocking curve $I_{ac}(\theta)$ and the scattering distribution $\rho(\theta)$ are convolved to produce the observed experimental intensity, $I_{exp}(\theta^*)$.

$$I_{exp}(\theta^*) = \int_{-\infty}^{\infty} I_{ac}(\theta^* - \theta)\rho(\theta)\, d\theta \qquad (1)$$

Convolution can also be written is terms of Fourier transforms,

$$F_{I_{exp}}(\omega) = F_{I_{ac}}(\omega)F_{\rho}(\omega) \qquad (2)$$

Where deconvolution is then

$$F_{\rho}(\omega) = \frac{F_{Iexp}(\omega)}{F_{I_{ac}}(\omega)} \qquad (3)$$

And the sample scattering distribution estimate is

$$\hat{\rho}(\theta) = F^{-1}\left(\frac{F_{Iexp}(\omega)}{F_{Iac}(\omega)}\right) \qquad (4)$$

Additive noise ε, which is statistically described via a Gaussian distribution, $N(\mu, \sigma^2)$, is always present in X-ray imaging. This means that both $I_{exp}(\theta^*)$ and $I_{ac}(\theta)$ respectively

contain additive random noise components ε_1 and ε_2. Such noise contributes to numerical instability of the direct Fourier inverse deconvolution method. To address this problem a range of deconvolution algorithms have been developed including Wiener deconvolution and t-SVD deconvolution, which can be very effective under low noise conditions.

The goal of this project is to accurately model the scattering distribution under high noise conditions, and to do this it is necessary to perform a deconvolution to separate the scattering component from the analyser rocking curve. In principle, modelling the scattering distribution should be easy, via Fourier Transform approaches, however as mentioned previously the presence of noise results in ill-conditioned numerical issues such as non-unique solutions and other numerical instabilities. As such a range of deconvolution algorithms have been developed, however the issue remains unresolved in general. Hence a different convolution method is proposed, which is to use wavelets.

Wavelets are mathematical representations of short wavelike oscillations, which can possess a variety of shapes. As a result of this, they can be highly optimised and can separate signal from noise. The discrete wavelet transform (DWT) decomposes a signal into set of 'smooth trend' coefficients $c_{j_0,k}$ and a set of 'detail' or 'change' coefficients, $d_{j,k}$, via the inner product of the signal I_{exp} with the respective scaling, $\phi_{j_0,k}$, and wavelet, $\psi_{j,k}$, basis functions. That is, $c_{j_0,k} = \langle I_{exp}, \phi_{j_0,k} \rangle$ and $d_{j,k} = \langle I_{exp}, \psi_{j,k} \rangle$ and the observed experimental intensity (I_{exp}) can be described via a linear combination of scaling and wavelet detail coefficients across locations and scales.

$$I_{exp} = \sum_k c_{j_0,k}\, \phi_{j_0,k} + \sum_{j \geq j_0} \sum_k d_{j,k}\, \psi_{j,k} \qquad\qquad (5)$$

Where $c_{j_0,k}$ are the scaling coefficients, $\phi_{j_0,k}$, the scaling function, $\psi_{j,k}$ referring to wavelet, j to resolution level, and k the translation coefficient (Fan & Koo, 2002). Wavelet thresholding operations on the detail coefficients has been demonstrated to be highly effective at removing additive Gaussian noise (Donoho & Johnstone, 1994). This project explores the concept of removing noise using wavelets prior to standard t-SVD deconvolution. This approach aims to recover a more accurate estimate of the scattering

AMSI

distribution, $\hat{\rho}(\theta)$, to be recovered from the deconvolution process under high levels of instrumentation noise. However, in order to see if wavelet deconvolution is successful, its performance must be compared to another deconvolution method under identical conditions.

In this project, Cecilia Andersson produced and analysed the results. Additionally, the report was written by Cecilia Andersson. Greg Falzon supervised the project, developed the MATLAB code, and helped with production and interpretation of the results.

Method

The experimental part of this project was completed entirely in MATLAB 2021b. Simulations were performed based on a model ABCI system, these simulations used observed experimental data but provided the benefit of providing exactly known quantities for numerical performance benchmarking. The first step was to simulate experimental intensity data, using a known rocking curve and scattering distribution and random additive Gaussian noise. Of course, in reality the scattering distribution is not known, but this way it is possible to compare the true distribution to the estimated. The observed experimental intensity can then be found via convolution of the analyser crystal rocking curve and the sample scattering distribution, with additive noise randomly sampled from numerical routines. The Pearson VII distribution function is known to be a good empirical fit to experimental rocking curve data, with the student t-distribution, a special case of the Pearson VII distribution, being accurate and logical to use as the analyser crystal rocking curve model. The sample scattering distribution was simulated using a Gaussian distribution model, which matches observational data from lung tissue (Kitchen et al., 2010; Zhong et al., 2003). Mathematically the noise-free analyser crystal rocking curve $\hat{I}_{ac}(\theta)$ can be modelled using the student t density function,

$$\hat{I}_{ac}(\theta) = \frac{1}{\pi(1+\theta)^2} \qquad (6)$$

Where $\frac{-\pi}{2} < \theta < \frac{\pi}{2}$, and the scattering distribution $\rho(\theta)$ can be modelled using the normal distribution,

$$\rho(\theta) = \frac{1}{\sigma\sqrt{2\pi}} e^{\frac{-(\theta-\mu)^2}{2\sigma^2}}$$ (7)

Figure 3 (a) and (b) respectively displays the simulated analyser crystal rocking curve and sample scatting distribution used in these experiments.
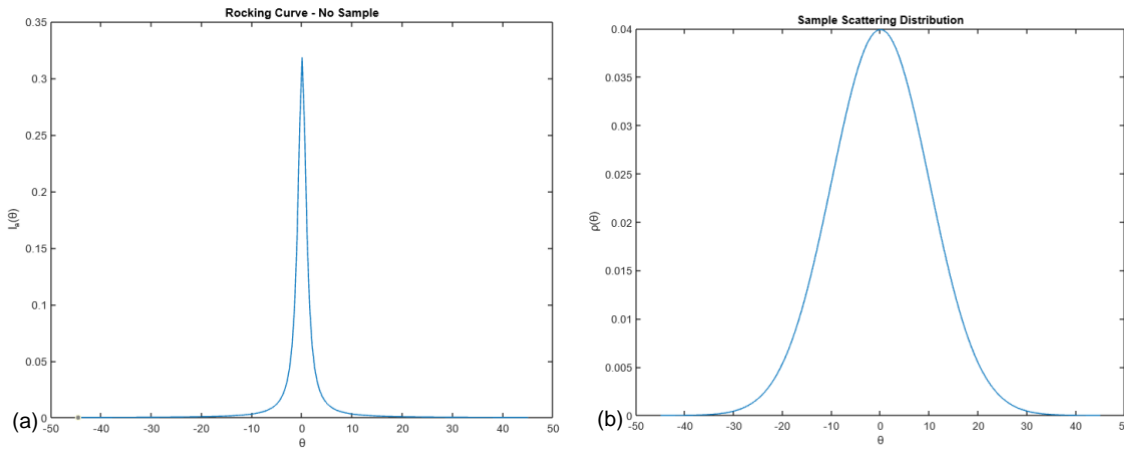

Figure 3: Images from the code producing simulated rocking curve data, where (a) shows the rocking curve and (b) shows the scattering distribution.

The simulated ABPCI system was modelled via inclusion of two components of independent and additive noise (ε_1, ε_2).

$$I_{exp} = I_{ac} * \rho + \varepsilon_1$$ (8)

$$I_{ac} = \hat{I}_{ac} + \varepsilon_2$$ (9)

Where $\varepsilon_1 \sim N(0, \sigma_1^2)$ and $\varepsilon_2 \sim N(0, \sigma_2^2)$, with the noise variances being described via parameters $\sigma_1^2 > 0$ and $\sigma_2^2 > 0$. In this model $\hat{I}_{ac}$ is noise free rocking curve and $*$ denotes convolution. Notably, the noise impacted rocking curve (I_{ac}) is used to simulate the observed experimental intensity (I_{exp}). This is a key characteristic of the analysis not addressed in current ABPCI deconvolution procedures. To perform deconvolution, the two error terms must be removed. As part of the algorithm, different levels of noise (σ_1^2, σ_2^2) were simulated.

Next step was to write a code to perform a deconvolution using one of the currently used methods. It was decided to do a T-SVD deconvolution, the t standing for truncated and SVD being singular value decomposition. A truncated SVD is essentially a reduced SVD which is simpler, faster and can remove noise from the system. It selects a subset of singular vectors, the largest ones, to provide a low-rank approximation to the convolution matrix operator, thereby hoping to avoid noise components (Huckle & Sedlacek, 2013). The t-SVD approach can be described as an inverse problem, hence providing a useful and tractable approach to the deconvolution problem.

Mathematically, the t-SVD deconvolution works as follows:

$$I_{exp} = \boldsymbol{A}_p + \varepsilon \tag{10}$$

Where $\boldsymbol{A} = \begin{bmatrix} a_0 & a_{-1} & \cdots & a_{-L} \\ a_1 & a_0 & \ddots & \vdots \\ \vdots & \ddots & \ddots & \vdots \\ a_L & \cdots & \cdots & a_0 \end{bmatrix}$, and each element is from I_{ac}. For example, $a_0 = I_{ac}(\theta)[0]$ is the first element of the analyser crystal rocking curve. The SVD is applied to $\boldsymbol{A}$,

$$\boldsymbol{A} = \boldsymbol{U}\boldsymbol{D}\boldsymbol{V}^{\mathrm{T}} \tag{11}$$

Only the top $\propto$ singular values are retained, corresponding to a low-rank (potentially noise free) system approximation,

$$\boldsymbol{D}_\propto = \begin{bmatrix} d_1 & & & & & \\ & d_2 & & & & \\ & & \ddots & & & \\ & & & d_\propto & & \\ & & & & \ddots & \\ & & & & & 0 \end{bmatrix}$$

A 'pseudo-inverse' operation can then be used to obtain $\hat{\rho}$ using the following equation.

$$\hat{\rho} = \boldsymbol{V}_\propto \boldsymbol{D}_\propto^{-1} \boldsymbol{U}_\propto^T I_{exp} \tag{12}$$

The next phase of the project involved creating a code to run wavelet deconvolution. It was decided to use a wavelet that belongs to the symlet family, symlet 4 (Daubechies, 1992). This approach involved removal of noise via wavelet thresholding, modification of wavelet transform coefficients. The prior removal of noise is expected to produce more stable and robust deconvolution results. Mathematically, this is described as follows

$$\hat{I}_{exp} = \sum_k c_{j_0,k}^{(1)} \phi_{j_0,k} + \sum_{j \geq j_0} \sum_k \hat{d}_{j,k}^{(1)} \psi_{j,k} \qquad (13)$$

$$\hat{I}_{ac} = \sum_k c_{j_0,k}^{(2)} \phi_{j_0,k} + \sum_{j \geq j_0} \sum_k \hat{d}_{j,k}^{(2)} \psi_{j,k} \qquad (14)$$

Where $\hat{d}_{j,k}$ is the noise removed wavelet coefficients (Fan & Koo, 2002). This was followed by the t-SVD deconvolution, the same as was used previously.

Results

The following images demonstrate the deconvolution comparisons across various noise level scenarios for one simulation.
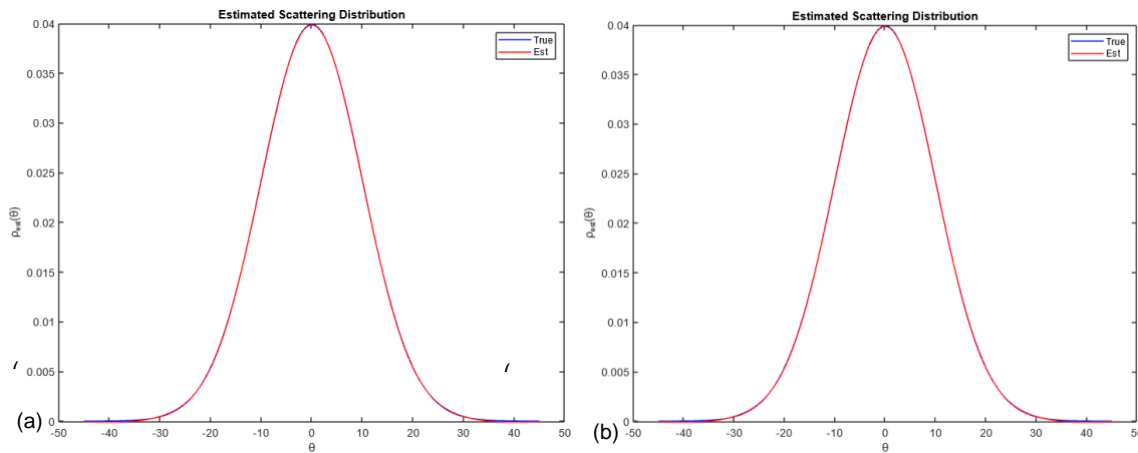

Figure 4: Graphs showing estimated scattering distribution from t-SVD deconvolution (a) and from Wavelet t-SVD deconvolution (b) with no noise.
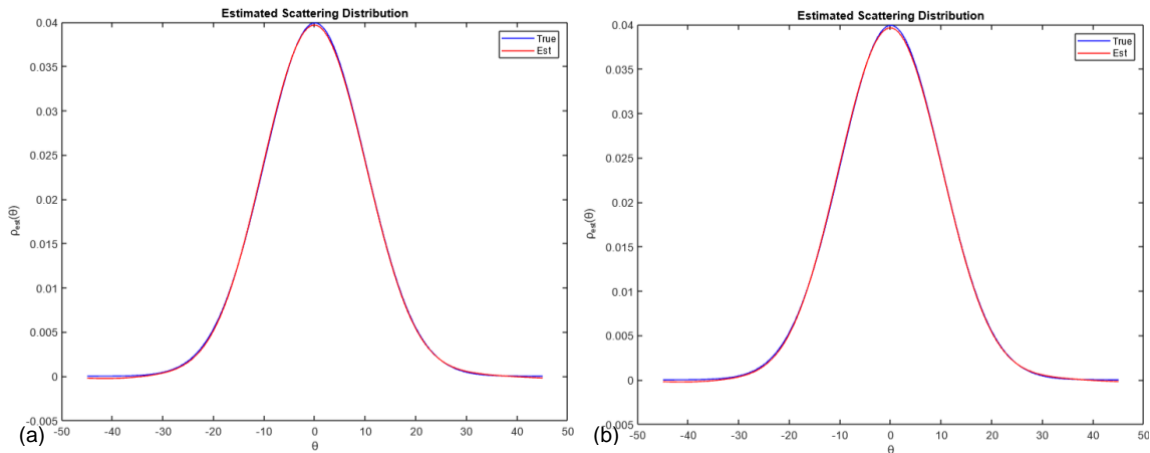
Figure 5: Graphs showing estimated scattering distribution from t-SVD deconvolution (a) and from Wavelet t-SVD deconvolution (b) under realistic conditions using current instrumentation.

For no noise and very low level of noise there are no discernible differences in performance between the algorithms. The estimated scattering distribution is virtually identical to the true distribution.
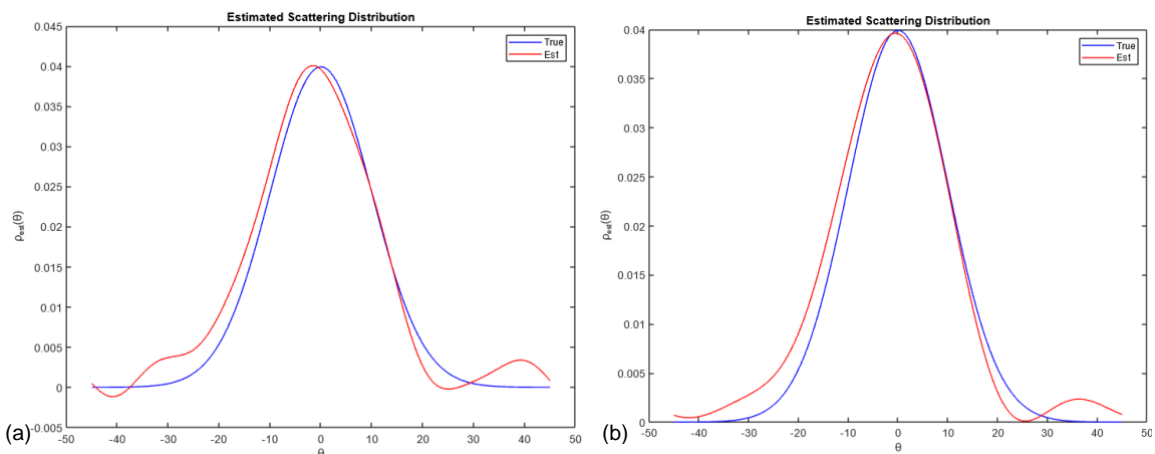

Figure 6: Graphs showing estimated scattering distribution from t-SVD deconvolution (a) and from Wavelet t-SVD deconvolution (b) with low level of noise.

For low noise, differences in performance start to appear. Most notably wavelet t-SVD deconvolution is slightly better at retaining the correct shape at extreme angles of θ.
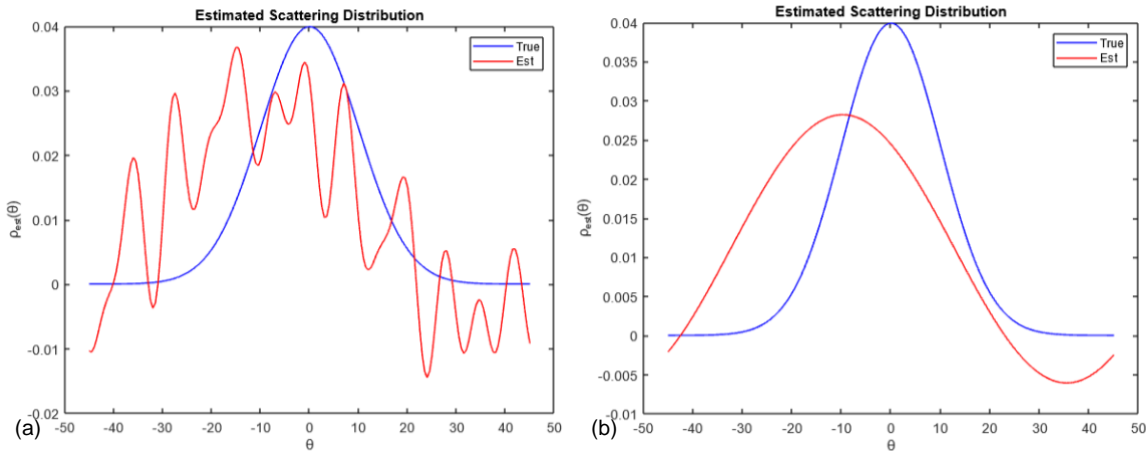
Figure 7: Graphs showing estimated scattering distribution from t-SVD deconvolution (a) and from Wavelet t-SVD deconvolution (b) with medium level of noise.
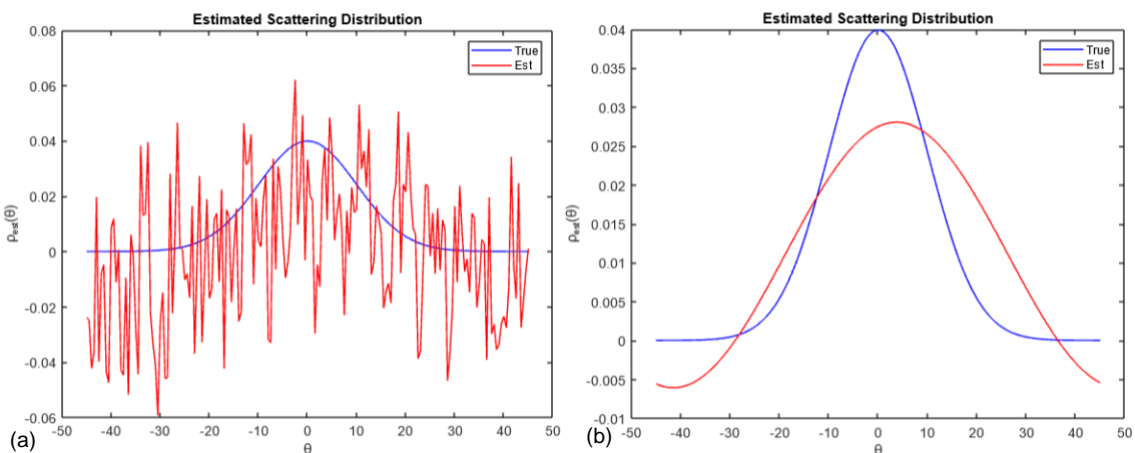

Figure 8: Graphs showing estimated scattering distribution from t-SVD deconvolution (a) and from Wavelet t-SVD deconvolution (b) with high level of noise.

For medium and high noise, the performances of the algorithms are highly different. The noise has rendered the reconstructed scattering distribution from t-SVD deconvolution largely meaningless, while the wavelet convolution algorithm has managed to mostly have the correct shape. In the table below the performances of the algorithms for varying levels of noise are summarised numerically, using root mean square error (RMSE).

Table 1: Root mean square error of the t-SVD algorithm's and the Wavelet t-SVD algorithm's performance in reconstructing the sample scattering distribution for different noise levels.

Noise level	σ^2	RMSE t-SVD	RMSE Wavelet t-SVD
None	0	0.2621	0.2621
Realistic conditions	0.001	0.2623	0.2623
Low	0.01	0.2613	0.2616
Medium	0.05	0.2904	0.2482
High	0.1	0.4220	0.2514

Discussion & Conclusion

Both qualitatively and quantitatively, it is evident that the wavelet deconvolution approach is more robust and able to obtain 'similar' scattering profiles under extremely high noise levels when the standard t-SVD approach is ineffective. Note that in current realistic conditions, both algorithms perform similarly, but this requires highly expensive equipment and higher X-ray doses. The wavelet t-SVD is very promising for high noise, which suggests that informative scattering information can be extracted under such conditions that might translate to much lower doses. Of course, these conclusions are drawn from a single simulation with limited statistical analysis, but at this stage, the aim was to find if using wavelets for deconvolution is a promising method, not determining its exact efficiency and accuracy.

Future work in this area should involve more extensive simulations across a range of imaging system models, scattering distributions and noise levels. A wider range of deconvolution algorithms need to be evaluated, along with modification to the current wavelet deconvolution algorithm. In particular, the widely used Wiener deconvolution should be evaluated. Finally, it would be beneficial to evaluate performance on real ABPCI data obtained from previous experiments.

References

Agrawal, A, Singh, B, Kashyap, Y, Shukla, M, Gakkari, SC 2017, 'Synchrotron-based X-ray microimaging facility for biomedical research', *Journal of Radiation and Cancer Research*, vol. 8, no. 3, pp. 153-159.

Bech, M, Tapfer, A, Velroyen, A, Yaroshenko, A, Pauwels, B, Hostens, J, Bruyndonckx, Sasov, A, Pfeiffer, F 2013, 'In-vivo dark field and phase-contrast x-ray imaging', *Scientific Reports*, vol. 3, 3209-3211.

Daubechies, I 1992, *Ten lectures on wavelets*, Society for Industrial and Applied Mathematics, Philadelphia, Pennsylvania.

Donoho, DL, & Johnstone, JM 1994, 'Ideal spatial adaptation by wavelet shrinkage', *Biometrika*, vol.81, no. 3, pp. 425-455.

Endrizzi, M 2018, 'X-ray phase-contrast imaging', *Nuclear Instruments and Methods in Physics Research*, vol. 878, pp. 88-98.

Fan, J, & Koo, JY 2002, 'Wavelet deconvolution', *IEEE transactions on information theory*, vol. 48, no. 3, pp. 734-747.

Huckle, T, Sedlacek, M 2013, 'Data based regularization for discrete deconvolution problems', *BIT Numerical Mathematics*, vol. 53, pp. 459-473.

Kitchen, M, Paganin, D, Uesugi, K, Allison, B, Lewis, R, Hooper, S, Pavlov, K 2010, 'X-ray phase, absorption and scatter retrieval using two or more phase contrast images', *Optics Express*, vol. 18, no. 19, pp. 19994-20012.

Pryor, E, Kitchen, M, Croughan, M, Crossley, K, Wallace, M, Lee, K, te Pas, A, McGillick, E, Hooper, S 2020, 'Improving lung aeration in ventilated newborn preterm rabbits with a partially aerated lung', *Journal of Applied Physiology*, vol. 129, pp. 891-900.

Taba, ST, Gureyev, TE, Alakhras, M, Lewis, S, Lockie, D, & Brennan, PC 2018, 'X-ray phase-contrast technology in breast imaging: principles, options, and clinical application', *American Journal of Roentgenology*, vol. 211, no.1, pp. 133-145.

Zhong, N, Morris, GM, Bacarian, T, Rosen, EM, Dilmanian, FA 2003, 'Response of Rat Skin to High-Dose Unidirectional X-Ray Microbeams: A Historical Study', *Radiation Research*, vol. 160, no. 2, pp. 133-142.

Zhou, S, Brahme, A 2008, 'Development of phase-contrast imaging techniques and potential medical applications', *Physica Medica*, vol. 24, pp. 129-148.